IEEE Access
Multidisciplinary | Rapid Review | Open Access Journal

Received 3 July 2024, accepted 22 July 2024, date of publication 29 July 2024, date of current version 8 August 2024.

*Digital Object Identifier 10.1109/ACCESS.2024.3434530*

RESEARCH ARTICLE

# Efficient Data Acquisition and Reconstruction in Ultrasound Imaging

**SAI KONDA, (Member, IEEE), AND HICHAM CHAOUI, (Senior Member, IEEE)**
Carleton University, Ottawa, ON K1S 5B6, Canada

Corresponding author: Sai Konda (saikonda@cmail.carleton.ca)

This work was supported in part by the Department of Electronics, Carleton University; and in part by the Centre for Innovative Ultrasound Solutions (CIRS), Norwegian Research Council.

**ABSTRACT** Ultrasound is a prominent imaging technique used in a variety of applications. Due to very high frame rate, the amount of raw data obtained while using an ultrasonic device is large. Thus, data management and storage are posing significant problems. To address these issues, we proposed and implemented a few efficient data acquisition, reconstruction, filtering, and noise removal techniques. These methods reduce the amount of raw data collection via hardware devices, followed by missing data reconstruction in the software using a variety of digital signal processing techniques such as Spline interpolation, Discrete Cosine Transform (DCT) and Inverse Discrete Cosine Transform (IDCT), Discrete Sine Transform (DST) and Inverse Discrete Sine Transform (IDST) etc., This reconstructed data is sent for Frequency Domain (FD) beamforming (a recently proposed beamforming technique) and post-processing to generate output images. For comparison, all outputs were generated using full data and Delay-and-Sum (DAS) beamforming (traditional beamforming technique in ultrasound). From which, it was clear that we can reduce the data storage cost by 33.3% and 50%, by increasing the software's operation time by a few seconds (i.e. less than one minute).

**INDEX TERMS** Ultrasound, spline interpolation, acoustical radiation force impulse (ARFI) imaging, delay-and-sum (DAS) beamforming, frequency domain (FD) beamforming, spline interpolation, discrete cosine transform (DCT), inverse discrete cosine transform (IDCT), discrete sine transform (DST), inverse discrete sine transform (IDST).

## I. INTRODUCTION

Ultrasonic imaging is famous for depth-based imaging. High frequency sound waves emitted from ultrasound scanner will penetrate the body of interest, hit the object of interest, and most of the waves will return to ultrasonic transducer elements as echo signals (i.e. data frames) [1]. Thus obtained data frames are either stored inside ultrasound machine or external storage device for further processing.

This imaging technique is so fast that it will generate thousands of data frames within a fraction of seconds [2]. Given this situation, data storage is presenting a major challenge.

We studied and closely observed various research works done in this area, some made use of data redundancy feature in ultrasound imaging. That is, techniques were developed to get rid of significant amount of channel data using a specified rule of thumb (which varies from one research work to another) and final images were generated using reduced data. As a result, finer and essential details were missing in output images.

One such work was done by Jian-yu [3], [4], which combined adjacent sensor data entries into a single entity to generate final images. Although they understood the relationship between image quality and data quantity, final images were generated with missing details. Recently proposed random subsampling method [5] by Junjin Yu down sampled the channel data in a randomized fashion and generated final output images with holes in the channel data. As a result, key features in the rat brain images were missing.

The associate editor coordinating the review of this manuscript and approving it for publication was Riccardo Carotenuto.

Novel works were done in the field of ultrasound imaging, related to channel data acquisition. Delcker and their team [6] proposed magnetic sensor data acquisition, which helped in imaging and measuring the diameter of optic nerve and lateral rectus muscle. Moeen Ud Din [7] and his team developed a hardware system for fingerprint data acquisition using ultrasound imaging. Another interesting hardware system was developed by Muhammad Nasir Ullah [8], which can collect ultrasound and gamma signals simultaneously using a common channel. Similar hardware systems were designed by Boni [9] and Chris [10], which acquire ultrasound raw data from multiple channels and store it in the onboard memory device.

Similarly, some research works are based on channel data compression to save storage costs. P. W. Cheng and his group [11], [12] proposed lossy data compression techniques for full channel data, which facilitated much faster data transfer from ultrasonic system to the processing computer. Channel data quantization was proposed by Daler to reduce the amount of data storage and transfer costs [13]. That is, entire channel data is encoded using a specially designed codebook. Values of this codebook are scaled based on raw channel data while encoding and decoding. Although it achieves good compression ratio, scaling algorithm changes with data, and designing a new codebook, encoding and decoding of channel data as per that codebook are added complexities in this technique.

However, some researchers believe that full data and kerf (distance between two adjacent sensors) are very crucial in ultrasound image formation. For example, Al-Hayani [14], who understood the relation between kerf and image quality, reduced kerf value in this work to generate output images using full data with utmost clarity. This covered several fine details of fetus phantom. Note that it comes with an expense of processing time and large amount of channel data.

Research work done by Marzougui [15] and Akbar [16] focused on emission angle based data reduction. In which, full zero-angle data was extracted for output image generation, non-zero angle data was either chosen or discarded, or subjected to subsampling based on similarity metrics such as Structural Similarity (SSIM) Index, Mean Square Error (MSE) etc., Although this provides scope for research in efficient angle based data extraction in ultrasound imaging, these techniques come with added computational complexity (due to similarity metrics calculation, data selection or rejection, downsampling etc.,), and lower overall image quality (due to missing raw data).

D'Souza [17] and Anjidani [18] focused on efficient speed of sound (SOS) wave calculation and neural network based ultrasound image enhancement respectively. While former focused on reducing the number of complex multiplications in SOS profiling by discarding spectrum values with smaller magnitude, the latter focused on designing a simple convolutional neural network for image enhancement. Image enhancement is important in the field of ultrasound (and our future scope).

Coming to data related issues in ultrasound imaging, Guo and his research group developed half matrix focusing method [19], assuming that the data is symmetric, upper triangular or lower triangular matrix in the data was discarded and final output images were generated. Because of which, 50% of channel data is lost. Moreover, final output image quality is poor, and Signal-to-Noise Ratio (SNR) value is low.

From above works, we learnt the effects of ignoring or reducing raw data content. This provided us with a scope to develop an ultrasound imaging technique, which will solve both data storage and image quality problems. Our plan is to develop efficient data acquisition techniques (which will save our data storage cost), followed by data reconstruction in the software (which will improve overall output image quality). Our contributions in this paper are listed as follows:

1) Proposed two efficient data acquisition techniques.
2) Explored various interpolation techniques in MATLAB and in image processing, applied 'Spline' interpolation on above techniques for data reconstruction, followed by noise filtering.
3) We also applied DCT/DST on efficient data acquisitions, performed appropriate zero padding on that transformed data, followed by IDCT/IDST to reconstruct missing data.
4) Calculated time taken for data reconstruction in the software, which is compared with percentage of memory saving in storage devices.
5) Applied recently proposed FD beamforming on reconstructed data and generated output images.
6) Resulting images and data were compared with that of ground truth (i.e. full data outputs via DAS beamforming), calculated various parameters to show that outputs obtained from proposed methods are very close to ground truth (with added savings in the raw data storage).
7) Simplified elastographic image generation process in Acoustical Radiation Force Impulse (ARFI) imaging, and then filtering the elastogram images for noise reduction and feature extraction.

This paper is structured as follows:

1) Introduction followed by related knowledge (which covers DAS and FD beamforming, simple elastographic image generation and filtering).
2) Proposed methods (which explain about all data acquisition and reconstruction methods), experimental results and analysis.
3) Conclusion and future work.

## II. RELATED KNOWLEDGE

### A. DELAY-AND-SUM (DAS) BEAMFORMING

DAS beamformer is the most basic and conventional beamforming technique in ultrasound. Ultrasonic signals sent by transducer elements will hit the target, and echo signals are received by elements at different time instants [20]. Appropriate timing delays are to be applied on echo signals

to keep them synchronous. Thus obtained time delayed echo signals are summed together to produce output signal [21].

In Fig.1, $\tau_1, \tau_2, \tau_3, \ldots, \tau_M$ represent timing delays, which are used to make sure that signals received from $M$ number of sensors are focused and processed accordingly. Here $m$ represents individual sensor. Thus obtained delayed signals $x_1[n], x_2[n], x_3[n], \ldots, x_M[n]$ get multiplied with corresponding weighting coefficients $w_1[n], w_2[n], w_3[n], \ldots, w_M[n]$ to form the outputs $y_1[n], y_2[n], y_3[n], \ldots, y_M[n]$. These individual outputs add together to generate final beamformed signal $y[n]$.

The weighting coefficients are fixed in non-adaptive DAS beamforming technique and are defined using window functions such as rectangular, Hanning, Kaiser etc., In this work, DAS beamformer works with rectangular window function. Thus, finally obtained beamformed output is represented using (1):

$$y[n] = \sum_{m=1}^{M} y_m[n] \tag{1}$$

### B. FREQUENCY DOMAIN (FD) BEAMFORMING

FD beamforming is a recently proposed beamforming technique [22], [23] to generate output images in ultrasound. 2D Fourier Transform was applied on the raw data in time $(x, t)$ domain, to obtain signal samples in frequency $(k_x, f)$ domain. In this method, $x$ means transducer element locations (i.e. spatial axis), $k_x$represent frequencies of spatial axis, $t$ is time axis and $f$ is temporal frequency. In the next step, $(k_x, f)$ data entries are translated into the $(k_x, k_z)$ domain via spectral interpolation.

Here, $k_z$ denotes the spatial frequencies in $z-$axis (which represent image depth). We apply 2D Inverse Fourier Transform on $(k_x, k_z)$ data to obtain beamformed data $P_e$ in $(x, z)$ domain.

Hilbert transform is applied on $P_e(x, z)$, and then complex conjugate is extracted from Hilbert's output, followed by final frequency domain interpolation to obtain final beamformed data $P_e(x, z)$.

### C. ELASTOGRAPHIC IMAGE GENERATION

Our proposed methods were applied on Acoustical Radiation Force Impulse (ARFI) imaging dataset [24] in ultrasound. This dataset imaged a sphere in spherical phantom [25] (see Fig. 6), whose young's modulus $E$ is greater than surrounding background. We generate elastographic images using displacement information and 2D shear wave speed. The former was calculated along with beamforming procedure, latter was obtained by using Time-to-Peak (TTP) technique coupled with a horizontally moving window of app. 4mm [26], [27], which will propagate on entire data frame. In TTP technique, we measure shear wave speed by performing linear regression on known data entities such as lateral distances and arrival times.

Lateral distance is the linear distance between a particular data point and the point where push force is exerted. Arrival time is the time instant when shear wave reaches/hits a particular data point. Note that the displacement value is highest when shear wave hits the data point. This TTP technique can be clearly explained using Fig. 4 and Fig. 5.

We have chosen five data points which are 2, 4, 6, 8 and 10 mm away from the push pulse. Fig. 4 shows displacement time profiles plotted for these five locations. Time instants at which displacement values are the highest are noted, these are arrival times. From the graph, arrival times for those locations are: 0.1667, 0.75, 1.083, 1.583, and 1.833 respectively. Since the propagation of shear wave is linear, we can calculate shear wave speed using following linear regression technique:

$$\boldsymbol{X} = \left(\begin{array}{c|c} x_1 & 1 \\ x_2 & 1 \\ x_3 & 1 \\ x_4 & 1 \\ x_5 & 1 \end{array}\right), \boldsymbol{Y} = \begin{pmatrix} y_1 \\ y_2 \\ y_3 \\ y_4 \\ y_5 \end{pmatrix}, \boldsymbol{W} = \begin{pmatrix} w \\ b \end{pmatrix}, \tag{2}$$

$$\boldsymbol{Y} = \boldsymbol{X}\boldsymbol{W} \tag{3}$$

Here $x_1$, $x_2$, $x_3$, $x_4$, $x_5$are lateral distances (i.e. 2, 4, 6, 8, 10 mm), $y_1$, $y_2$, $y_3$, $y_4$, $y_5$are arrival times calculated from graph (Fig. 4). (i.e. 0.16, 0.75, 1.08, 1.58, 1.83 ms). To calculate $\boldsymbol{W}$ (i.e. slope $w$ and $y-$intercept $b$), the governing equation is:

$$\boldsymbol{W} = (\boldsymbol{X}^{\mathrm{T}}\boldsymbol{X})^{-1}(\boldsymbol{X}^{\mathrm{T}}\boldsymbol{Y}) \tag{4}$$

The value of $1/w$ is our required shear wave speed $c_T$. Square of that obtained shear wave speed value will result in shear modulus $(\mu)$.

The relationship between shear modulus $(\mu)$ and young's modulus $(E)$ is shown in (5) [28]. Thus calculated $E$ value will replace center pixel in the window and procedure will continue for entire data frame. The resulting output image is our elastogram.

In [29], elastographic images were initially generated using various window sizes, averaging all of them to generate a final elastographic image. However, in our work we have chosen a reasonable window size which was able to generate good quality elastographic images. Because of which, we were able to reduce unnecessary calculations in elastographic image generation. This makes our elastogram algorithm work computationally faster. Mean and median filters were applied on this above elastographic image to generate final elastograms with utmost clarity. These elastograms were able to show the sphere in output images.

$$E = 3\mu \tag{5}$$

## III. PROPOSED METHODS

### A. EFFICIENT DATA ACQUISITION TECHNIQUES

When we conduct a research study on efficient data acquisition techniques, an obvious question from the crowd would be, what is the need for efficient data acquisition when full data and current imaging techniques are working fine? The answer to this question is, less data acquisition has

benefits such as lower ultrasonic device operating time, memory storage, power utilization, heat dissipation etc.,. Hence, we propose two efficient data acquisition techniques based on temporal sampling rate reduction, which are as follows:

#### 1) REDUCE SAMPLING RATE BY 2/3

By reducing the temporal sampling rate of ultrasonic transducer by 2/3, we will collect two rows of raw data out of every three rows. In this way, we can collect 66.6% of channel data using ultrasonic transducer and ignore 33.3% of the data.

#### 2) REDUCE SAMPLING RATE BY 1/2

In the second technique, we reduce the temporal sampling rate of ultrasonic transducer by 1/2, i.e. we will collect one row out of every two rows, will ignore every second row. In this way, we can collect 50% of channel data using ultrasonic transducer and ignore the remaining 50% of the data. Fig. 2 and Fig. 3 will explain these data reduction techniques more clearly.

$D_{Ntn}$ denotes data point acquired at time instant Nt and sensor position n. Bold and ruled out rows are neglected in raw data acquisition.

### B. EFFICIENT DATA RECONSTRUCTION METHODS

Raw data collected in 3-1 and 3-2 (i.e. above sections) can be sent as an input to ultrasonic image processing software, where software will reconstruct missing data and will perform further operations on new data. In this work, we propose two data reconstruction techniques:

#### 1) NORMAL IMAGE INTERPOLATION

We applied various interpolation techniques [30] on raw data collected from 3-1 and 3-2. Among all those techniques, 'Spline' interpolation gave us better and reliable results. Spline interpolation values are calculated based on cubic interpolation of data points in the neighboring grid points in that corresponding dimension. Note that cubic interpolation is based on cubic convolution of nearest data points. And so, we have chosen spline interpolation in MATLAB to reconstruct the missing data. Our methods and their outputs are named as (2/3 Spline + FD) and (1/2 Spline + FD) beamforming respectively. Here 2/3 and 1/2 represent temporal sampling rate. The following are the steps which explain this reconstruction technique:

1) Take subsampled data matrix as an input, reshape the matrix (i.e. convert 2D data frame into 1D data).
2) Apply appropriate interpolation operation on 1D data using 'interp' function, set the method as 'spline', to reconstruct the missing data.
3) Thus, obtained data is passed through image processing and noise elimination filters to filter the reconstructed data.
4) We calculated the time taken by software to perform the above steps 1, 2, and 3.
5) This filtered data is sent to ultrasonic image processing system to generate all the required outputs.

In real time applications, higher order polynomial-based interpolation techniques are not commonly used, due to their complexity. Moreover, their results are almost equivalent to (and sometimes not better than) spline (i.e. piecewise interpolation). And so, linear and cubic spline techniques are popularly used for interpolation problems.

Mathematical equation governing this linear spline is given below:

$$I_K(v) = I_k + (I_{k+1} - I_k)(V - V_k)/(V_{k+1} - V_k) \quad (6)$$

(6) is a linear line segment between the two points $(V_k, I_k)$ and $((V_{k+1}, I_{k+1})$.

In general, linear interpolation reconstruction does not consider slopes and inclinations of a curve. And so, we have chosen cubic splines for more accurate reconstruction. The main equation for cubic spline interpolation is:

$$I_K(v) = I_k + a_k (V - V_k) + b_k(V - V_k)^2 + c_k(V - V_k)^3 \quad (7)$$

The boundary or limiting conditions in (7), $a_k$, $b_k$ and $c_k$ are:

$$a_k = \frac{I_{k+1} - I_k}{V_{k+1} - V_k} - \frac{(2m_k + m_{k+1})(V_{k+1} - V_k)}{6} \quad (8)$$

$$b_k = 0.5\, m_k \quad (9)$$

$$c_k = \frac{(m_{k+1} - m_k)}{6(V_{k+1} - V_k)} \quad (10)$$

Here, $V = [V_k, V_{k+1}]$ and $k = 0, 1, \ldots, (n\text{-}1)$.

#### 2) MISSING DATA RECONSTRUCTION USING COSINE AND SINE TRANSFORMS

In this technique, we are using Discrete Cosine Transform (DCT), Inverse Discrete Cosine Transform (IDCT) or Discrete Sine Transform (DST), Inverse Discrete Sine Transform (IDST) [30] functions in MATLAB to reconstruct the missing data in 3-2. These methods are explained in following sections:

##### a: DCT, IDCT/DST, IDST BASED DATA RECONSTRUCTION

In this method, we are applying either 1D DCT or 1D DST on the missing data (3)-(2), followed by appropriate zero padding. Zero padding is a technique to add zeros at the end of the signal sample to match the size of full data frame. After which, we perform 1D IDCT or 1D IDST on that zero padded data frame, which will reconstruct the missing data. In this way, we will reconstruct 50% of that missing data.

##### b: DISCRETE COSINE TRANSFORM (DCT)

DCT is used to represent data points as a sum of cosine functions oscillating at different frequencies. Using DCT, we will be able to separate the image into various spectral bands.

The equation for 1D DCT for an $N$-sampled signal $f[n]$ is:

$$F[v] = \sqrt{\frac{2}{N}} c[v] \sum_{n=0}^{N-1} f[n] \cos\left(\frac{\pi(2n+1)v}{2N}\right), \quad 0 \le v \le N-1 \quad (11)$$

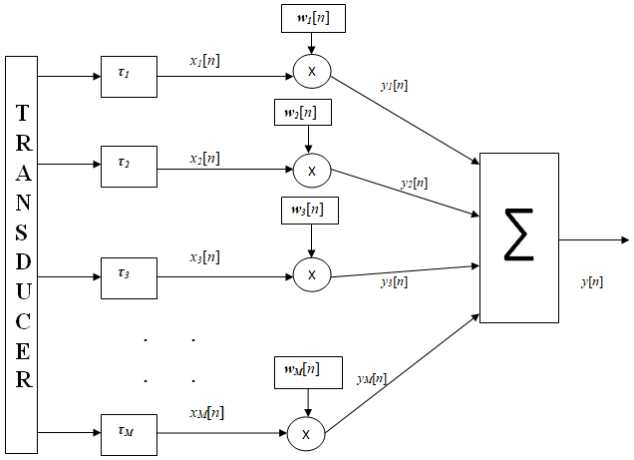


**FIGURE 1.** DAS beamformer.

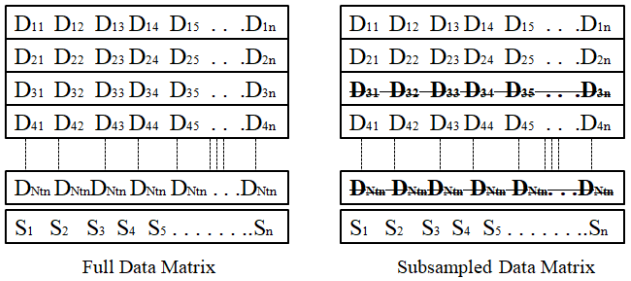


**FIGURE 2.** Data matrix subsampled by 2/3.

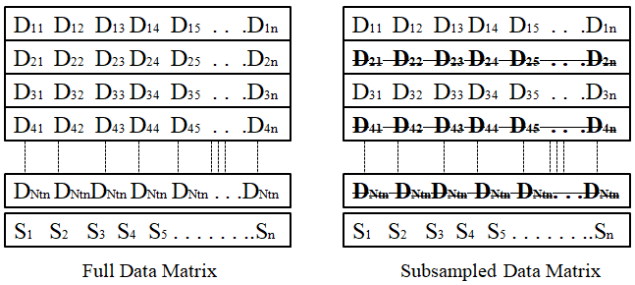


**FIGURE 3.** Data matrix subsampled by 1/2.

Here $n$ is a sampling time instant, and c[$v$]is a normalization factor, which is defined by:

$$c[v] = \begin{cases} 1/\sqrt{2}, & v = 0 \\ 1, & otherwise \end{cases} \tag{12}$$

The recovered/reconstructed signal $f[n]$ can be obtained from $F[v]$ using 1D IDCT:

$$f[n] = \sum_{v=0}^{N-1} c[v] F[v] \times cos\left(\frac{\pi(2n+1)v}{2N}\right), \; 0 \leq v \leq N-1 \tag{13}$$

### c: DISCRETE SINE TRANSFORM (DST)

DST is also another transform in the field of signal processing, which is used to represent data points as a sum of sine functions.

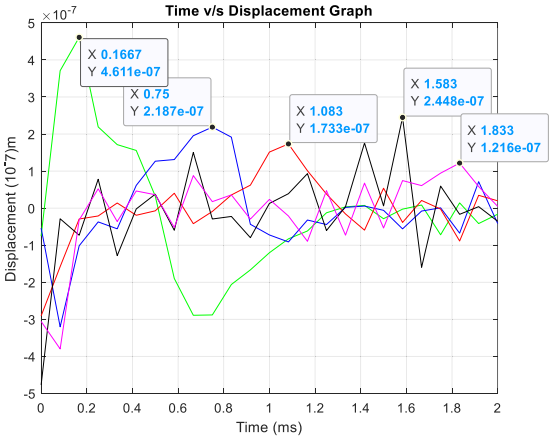


**FIGURE 4.** Displacement time profile plotted for five chosen locations at various distances (2, 4, 6, 8, and 10 mm) away from the push. The first green peak (at 0.1667 ms), second blue peak at (0.75 ms), third red peak (at 1.083 ms), fourth black peak (at 1.583 ms), and fifth magenta peak (at 1.833 ms) correspond to the locations that are 2, 4, 6, 8, and 10 mm away from the push, respectively.

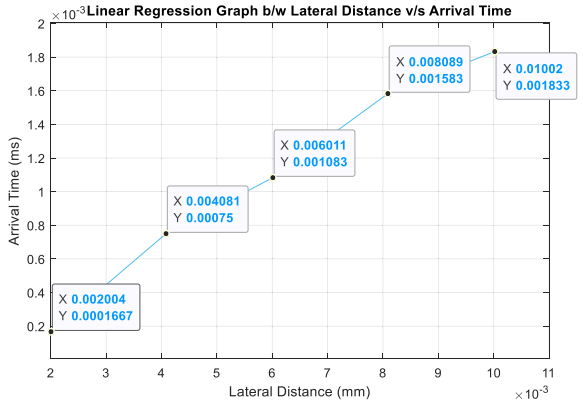


**FIGURE 5.** Linear regression graph for 5-data points.

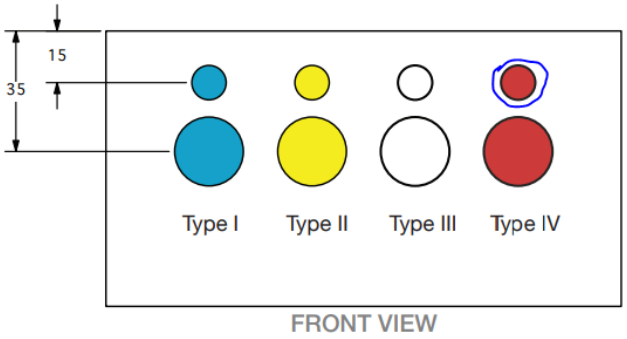


**FIGURE 6.** Front view of CIRS spherical phantom [25].

The equation for 1D DST for an $N$-sampled signal $x[n]$ is:

$$Xk = \sum_{n=0}^{N-1} x[n] \, sin\left(\frac{\pi(n+1)(k+1)}{N+1}\right), \quad k = 0, \ldots, N-1 \tag{14}$$

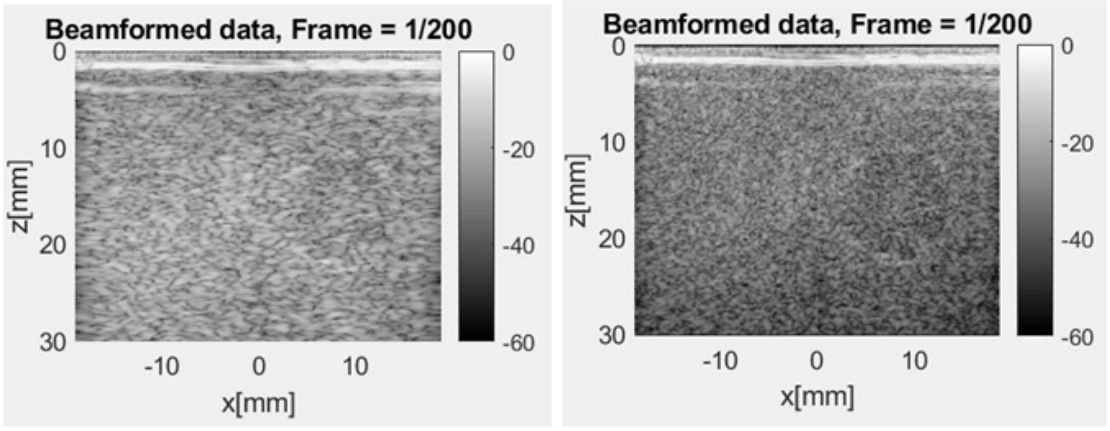


**FIGURE 7.** B-mode images for DAS and FD beamforming.

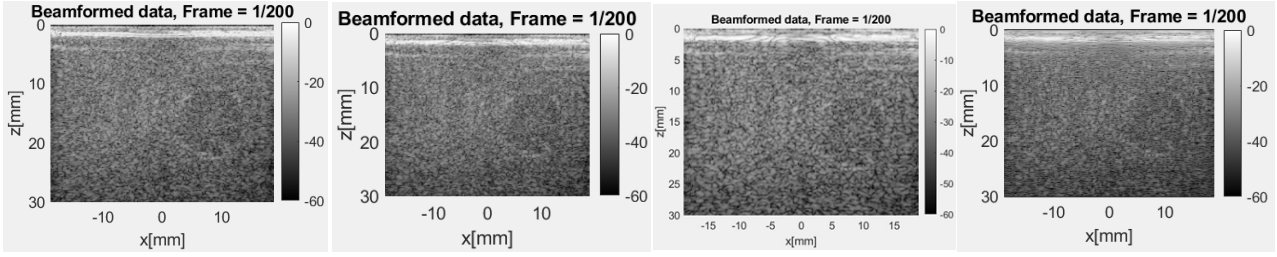


**FIGURE 8.** B-mode images for (2/3 Spline + FD), (1/2 Spline + FD), (DCT + FD) and (DST + FD).

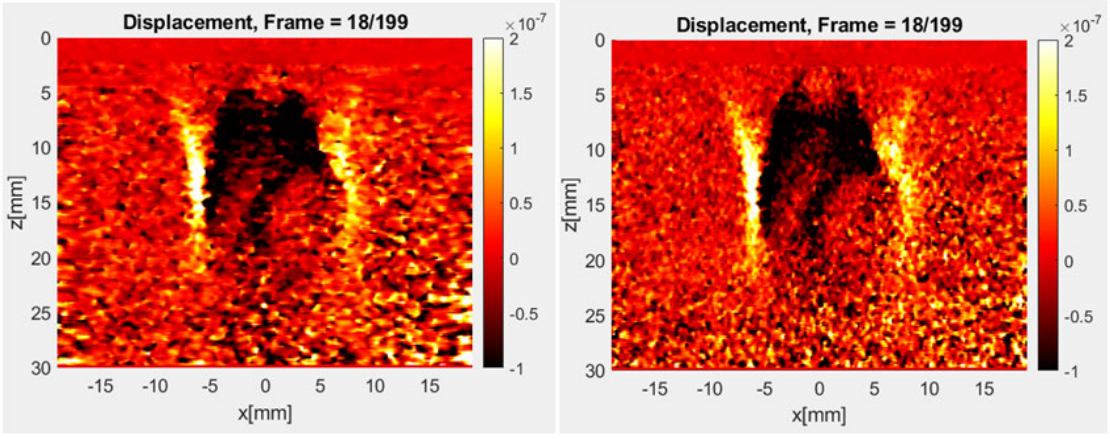


**FIGURE 9.** Displacement images for DAS and FD beamforming for frame# 18.

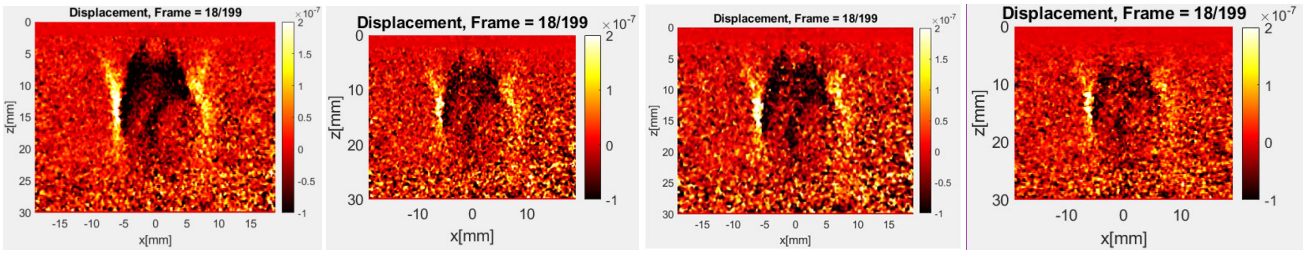


**FIGURE 10.** Displacement images for (2/3 Spline + FD), (1/2 Spline + FD), (DCT + FD) and (DST + FD) for frame# 18.

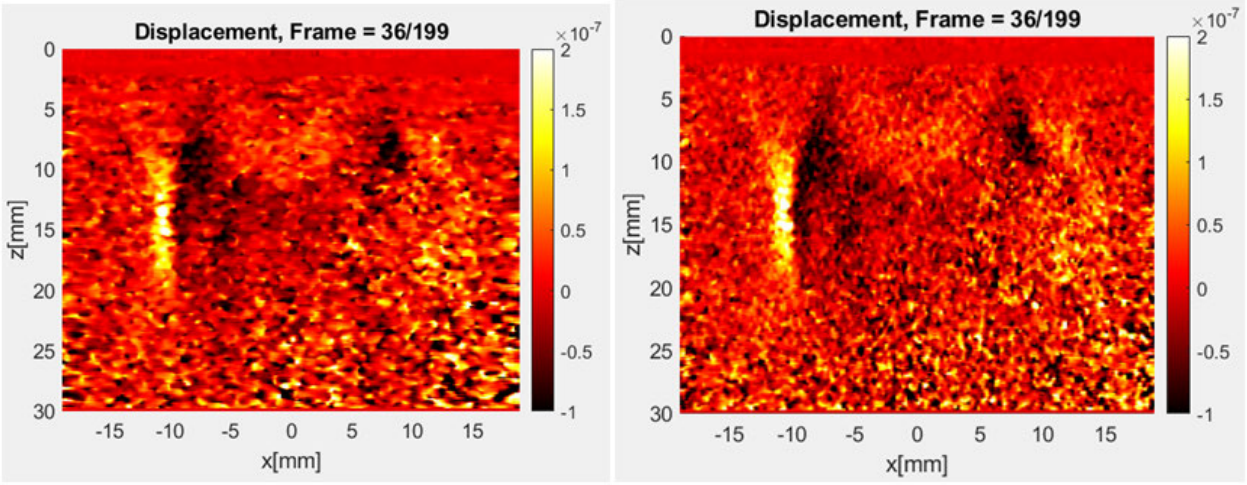


**FIGURE 11.** Displacement images for DAS and FD beamforming for Frame# 36.

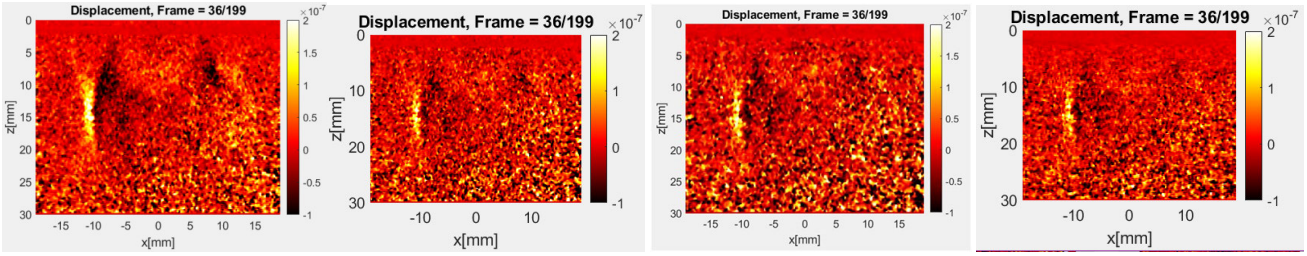


**FIGURE 12.** Displacement images for (2/3 Spline + FD), (1/2 Spline + FD), (DCT + FD) and (DST + FD) for frame# 36.

**TABLE 1.** Structural Similarity Metric (SSIM) calculations for displacement images for FD (recently proposed), (2/3 Spline + FD), (1/2 Spline + FD), (DCT + FD), (DST + FD) beamforming.

| Frame# | SSIM b/w DAS (Ref) and FD Images | SSIM b/w FD (Ref) and (2/3 Spline + FD) | SSIM b/w FD (Ref) and (1/2 Spline + FD) | SSIM b/w FD (Ref) and (DCT + FD) | SSIM b/w FD (Ref) and (DST + FD) |
|---|---|---|---|---|---|
| Frame 6 | 0.9404 | 0.9909 | 0.8900 | 0.9077 | 0.8934 |
| Frame 12 | 0.9473 | 0.9913 | 0.8965 | 0.9149 | 0.9019 |
| Frame 18 | 0.9482 | 0.9914 | 0.9012 | 0.9226 | 0.9126 |
| Frame 24 | 0.9515 | 0.9917 | 0.9038 | 0.9203 | 0.9178 |
| Frame 30 | 0.9503 | 0.9921 | 0.9053 | 0.9207 | 0.9201 |
| Frame 36 | 0.9516 | 0.9924 | 0.9037 | 0.9199 | 0.9196 |
| Frame 42 | 0.9524 | 0.9923 | 0.9073 | 0.9248 | 0.9226 |

Here $n$ is a sampling time instant, the recovered/reconstructed signal $x[n]$ can be obtained from $Xk$ using 1D IDCT:

$$x[n] = \frac{2}{N+1} \sum_{k=1}^{N} Xk \,.\, sin\left(\frac{\pi kn}{N+1}\right), n = 1, \ \ldots, \ N \tag{15}$$

*d: RECONSTRUCTION/INTERPOLATION WITH ZERO PADDING*

In the theory of digital signal processing, zero padding in frequency domain will result in interpolation in the time domain $f\ [n]$. That is:

$$INTERP_{L,N}(f) = IDCT(2 \cdot ZEROPAD_{L,N}(F)) \tag{16}$$

**TABLE 2.** Image Mean Square Error (IMMSE) calculations for displacement images for FD (recently proposed), (2/3 Spline + FD), (1/2 Spline + FD), (dct + fd), (dst + fd) beamforming.

| Frame# | IMMSE b/w DAS (Ref) and FD Images | IMMSE b/w FD (Ref) and (2/3 Spline + FD) | IMMSE b/w FD (Ref) and (1/2 Spline + FD) | IMMSE b/w FD (Ref) and (DCT + FD) | IMMSE b/w FD (Ref) and (DST + FD) |
|---|---|---|---|---|---|
| Frame 6 | $2.8224*10^{-5}$ | $4.1979*10^{-6}$ | $3.4922*10^{-5}$ | $3.8259*10^{-5}$ | $4.4813*10^{-5}$ |
| Frame 12 | $2.2957*10^{-5}$ | $3.8632*10^{-6}$ | $3.0350*10^{-5}$ | $3.4322*10^{-5}$ | $3.7841*10^{-5}$ |
| Frame 18 | $2.1465*10^{-5}$ | $3.5587*10^{-6}$ | $2.7260*10^{-5}$ | $2.9838*10^{-5}$ | $2.9491*10^{-5}$ |
| Frame 24 | $2.0061*10^{-5}$ | $3.3744*10^{-6}$ | $2.5757*10^{-5}$ | $2.9152*10^{-5}$ | $2.7209*10^{-5}$ |
| Frame 30 | $1.9274*10^{-5}$ | $3.1416*10^{-6}$ | $2.4506*10^{-5}$ | $2.7839*10^{-5}$ | $2.6103*10^{-5}$ |
| Frame 36 | $1.8629*10^{-5}$ | $3.0943*10^{-6}$ | $2.4675*10^{-5}$ | $2.8269*10^{-5}$ | $2.5741*10^{-5}$ |
| Frame 42 | $1.9027*10^{-5}$ | $3.1660*10^{-6}$ | $2.4504*10^{-5}$ | $2.7484*10^{-5}$ | $2.4985*10^{-5}$ |

**TABLE 3.** Peak signal to noise ratio (PSNR) calculations for displacement images for FD (recently proposed), (2/3 Spline + FD), (1/2 Spline + FD), (DCT + FD), (DST + FD) beamforming.

| Frame# | PSNR b/w DAS (Ref) and FD Images | PSNR b/w FD (Ref) and (2/3 Spline + FD) | PSNR b/w FD (Ref) and (1/2 Spline + FD) | PSNR b/w FD (Ref) and (DCT + FD) | PSNR b/w FD (Ref) and (DST + FD) |
|---|---|---|---|---|---|
| Frame 6 | 145.4939 | 153.7696 | 144.5690 | 144.1727 | 143.4860 |
| Frame 12 | 146.3908 | 154.1305 | 145.1783 | 144.6443 | 144.2203 |
| Frame 18 | 146.6828 | 154.4871 | 145.6448 | 145.2523 | 145.3031 |
| Frame 24 | 146.9764 | 154.7180 | 145.8910 | 145.3534 | 145.6528 |
| Frame 30 | 147.1503 | 155.0284 | 146.1072 | 145.5535 | 145.8331 |
| Frame 36 | 147.2980 | 155.0943 | 146.0774 | 145.4868 | 145.8937 |
| Frame 42 | 147.2063 | 154.9949 | 146.1076 | 145.6092 | 146.0231 |

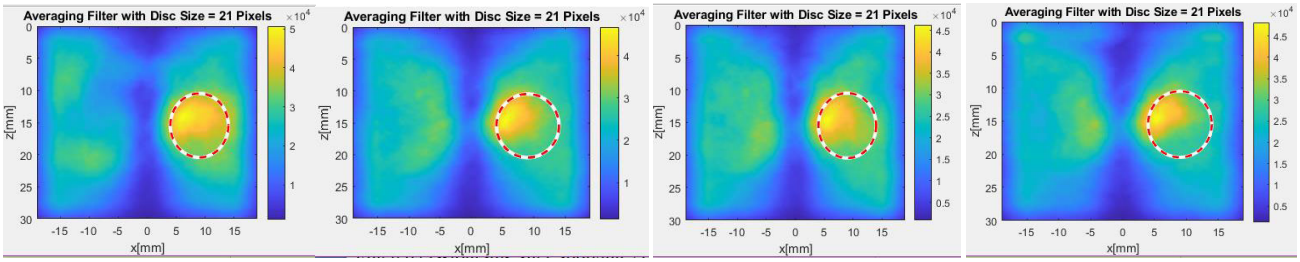


**FIGURE 13.** Filtered elastograms after applying 21-pixel disc averaging for (2/3 Spline + FD), (1/2 Spline + FD), (DCT + FD) and (DST + FD).

Here:

$$ZEROPAD_{L,N}(F) = \begin{cases} F[v], 0 \leq v < N \\ 0, N \leq v < L \cdot N \end{cases} \quad (17)$$

In our work, we are zero padding the DCT output $\boldsymbol{F}[v]$ by a factor $\boldsymbol{L} = \mathbf{2}$ and will perform IDCT to reconstruct missing data. Please note that DCT and IDCT in this section can be replaced with DST and IDST.

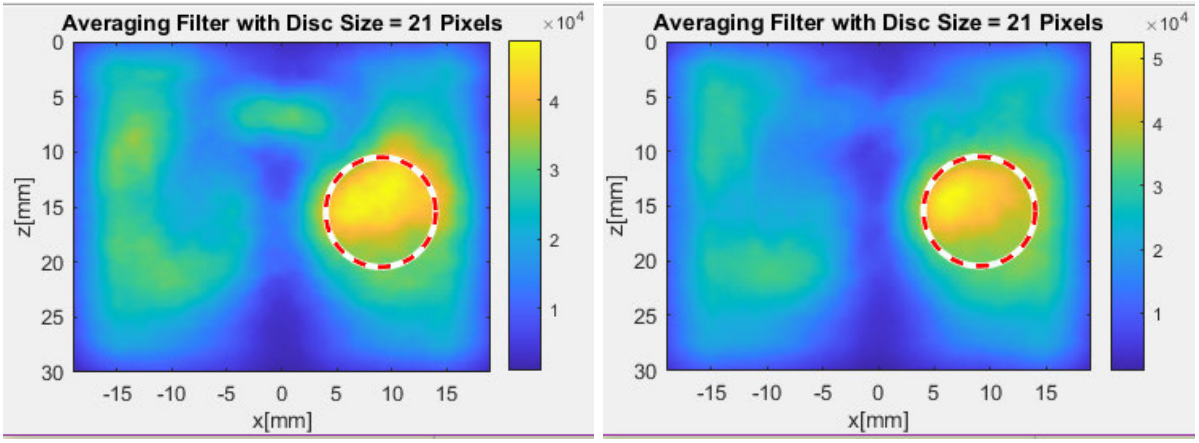


**FIGURE 14.** Filtered elastograms after applying 21-pixel disc averaging for DAS and FD beamforming.

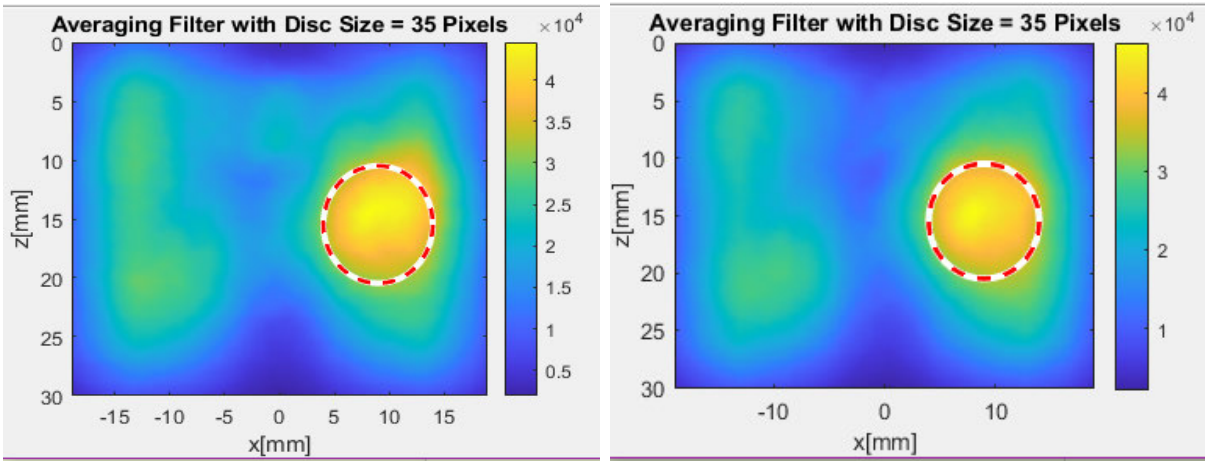


**FIGURE 15.** Filtered elastograms after applying 35-pixel disc averaging for DAS and FD beamforming.

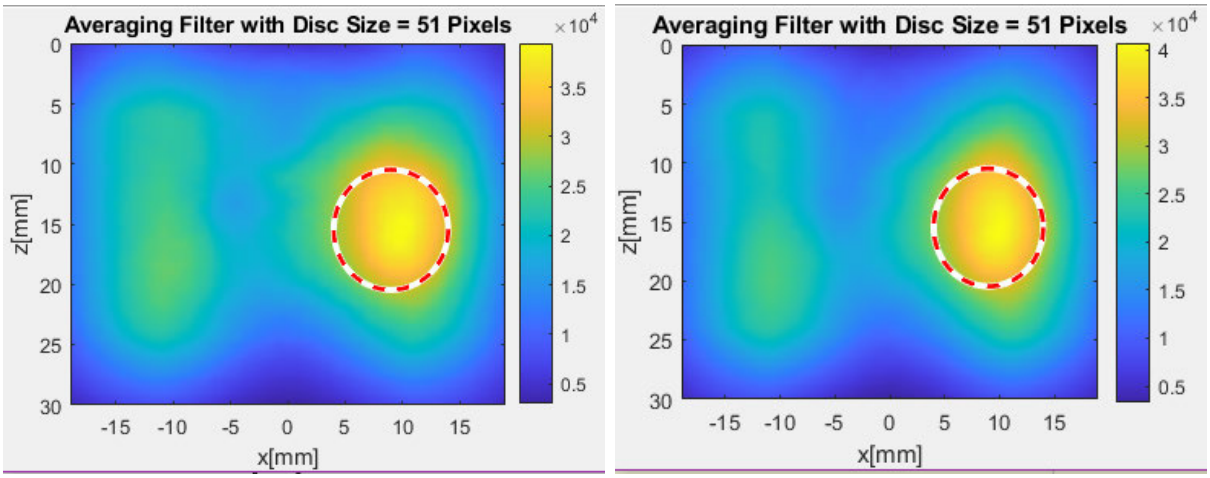


**FIGURE 16.** Filtered elastograms after applying 51-pixel disc averaging for DAS and FD beamforming.

This reconstructed data is sent for ultrasonic image processing and final output generation. Please note that our methods are named as (DCT + FD) and (DST + FD) beamforming respectively.

## IV. EXPERIMENTAL RESULTS AND ANALYSIS

Fig. 7 presents DAS and FD beamformed images for sphere in CIRS spherical phantom. In DAS image, the sphere is seen like a black shadow in the right side of the image.

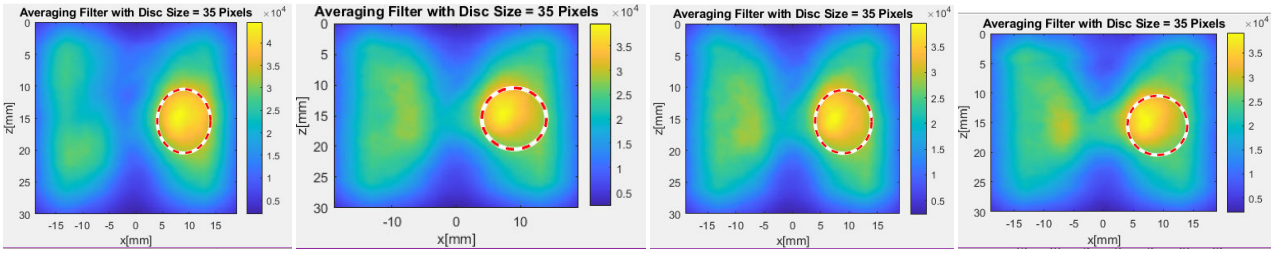


**FIGURE 17.** Filtered elastograms after applying 35-pixel disc averaging for (2/3 Spline + FD), (1/2 Spline + FD), (DCT + FD) and (DST + FD).

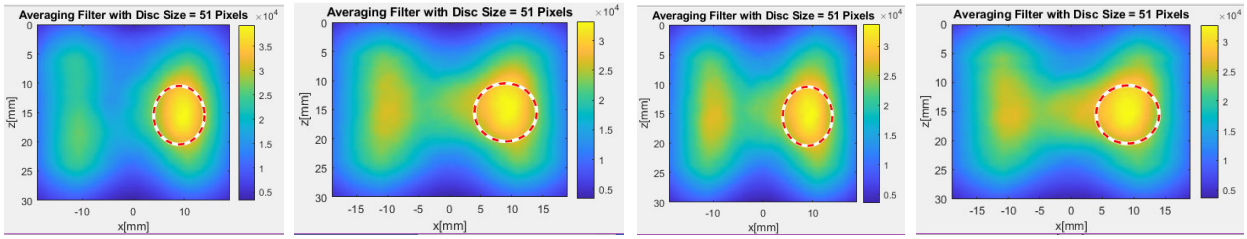


**FIGURE 18.** Filtered elastograms after applying 51-pixel disc averaging for (2/3 Spline + FD), (1/2 Spline + FD), (DCT + FD) and (DST + FD).

**TABLE 4.** Structural Similarity Metric (SSIM) calculations for elastogram images for FD (recently proposed), (2/3 Spline + FD), (1/2 Spline + FD), (DCT + FD), (DST + FD) beamforming.

| Disc - 21 | | | | | |
|---|---|---|---|---|---|
| Metric | **SSIM b/w DAS (Ref) and FD Images** | **SSIM b/w FD (Ref) and (2/3 Spline + FD)** | **SSIM b/w FD (Ref) and (1/2 Spline + FD)** | **SSIM b/w FD (Ref) and (DCT + FD)** | **SSIM b/w FD (Ref) and (DST + FD)** |
| SSIM | 0.9608 | 0.9898 | 0.9471 | 0.9488 | 0.9203 |
| **Disc - 35** | | | | | |
| | **SSIM b/w DAS (Ref) and FD Images** | **SSIM b/w FD (Ref) and (2/3 Spline + FD)** | **SSIM b/w FD (Ref) and (1/2 Spline + FD)** | **SSIM b/w FD (Ref) and (DCT + FD)** | **SSIM b/w FD (Ref) and (DST + FD)** |
| SSIM | 0.9869 | 0.9976 | 0.9754 | 0.9769 | 0.9638 |
| **Disc - 51** | | | | | |
| | **SSIM b/w DAS (Ref) and FD Images** | **SSIM b/w FD (Ref) and (2/3 Spline + FD)** | **SSIM b/w FD (Ref) and (1/2 Spline + FD)** | **SSIM b/w FD (Ref) and (DCT + FD)** | **SSIM b/w FD (Ref) and (DST + FD)** |
| SSIM | 0.9946 | 0.9991 | 0.9874 | 0.9769 | 0.9820 |

However, boundary of the sphere is clearly noticeable in FD beamforming. Sphere boundary is also seen in all the Fig. 8 images. From which it is clear that:

1) FD beamforming is better than DAS, which can generate final images with more clarity and sharpness.
2) Fig. 8 images were obtained after performing efficient data acquisition and data reconstruction. Still, these outputs are far better compared to conventional DAS technique.

Our (2/3 Spline + FD) and (1/2 Spline + FD) methods take approximately 32s for 33.3% and 50% data reconstruction, our (DCT + FD) and (DST + FD) methods take approximately 0.7s and 3.8s respectively for 50% data recovery. From which, it is evident that proposed methods are more efficient compared to conventional techniques.

Fig. 9, Fig. 10, Fig. 11, and Fig. 12 show displacement time frame images for frame# 18 and 36 for both reference methods and our techniques. Visually all images in Fig. 9

and Fig. 10 look alike, and images in Fig. 11 and Fig. 12 look similar. However, it's always a better idea to calculate image metrics, so we can be confident about results.

We present SSIM, Image Mean Square Error (IMMSE) and Peak Signal to Noise Ratio (PSNR) values [31] for displacement images in tables 1, 2, and 3. SSIM values are in the range of 0.89 to 0.99, IMMSE values are very low (i.e. in the order of $10^{-5}$and $10^{-6}$), PSNR values are in the range of 145 to 155.

Fig. 13 to Fig. 18 display filtered elastogram images after applying averaging filters with disc sizes 21, 35 and 51 pixels on elastographic image data, alternating white and red colored circle in the images represent actual sphere. The thick yellow patch inside that circle is the sphere we imaged using our practical approach.

Our elastogram images obtained from averaging filters of 35 and 51 pixels are better (i.e. three-fourth of the circle is filled with yellow color) compared to that of 21pixels (where only a portion of the circle is yellow). SSIM values calculated for all the elastographic images (available in table 4) are in the range of 0.92 to 0.99.

## V. CONCLUSION AND FUTURE WORK

In our literature study, we inspected a good number of techniques in ultrasound imaging, related to data acquisition, data compression etc., While some techniques used data redundancy feature in ultrasound imaging to reduce the amount of raw data for final image generation, others focused on data compression for data storage and transfer. Some of the techniques were based on emission angle based efficient data acquisition. However, these techniques did not focus on missing data reconstruction for output image generation. As a result, key details were missing in output images. Please note that, although Daler's technique is an exception to above, it comes with an expense of designing a new code book for encoding the channel data and scaling it (where, scaling is data dependent), and decoding it in the end.

In our work, we focused on both efficient data acquisition and missing data reconstruction for final image generation, which will overcome all the image and data related issues in above techniques. As a result, all our output images (i.e. b-mode, displacement and elastographic images) and image comparison metrics (such as SSIM, IMMSE and PSNR) are in very close resemblance with conventional techniques.

In this work, we presented two efficient data acquisition and three data reconstruction techniques. When we compare the results of our methods with standard techniques, we noticed that our techniques are more efficient and are offering the advantage of data savings up to 50%. Since the amount of data acquisition by ultrasonic device and transducer got reduced by half, the device's operation time is also reduced by half.

We know that device operation time of ultrasonic system is directly proportional to some of the factors such as power consumption, heat dissipation, system usage, sensor operational lifetime etc., With our technique, if the former aspect got reduced by 50%, then all the latter factors will also reduce by same amount, which will increase ultrasonic system's life time as a whole.

Our techniques can save 50% storage space in memory devices, which comes with an expense of very low data reconstruction software time lapse (which is minimum for DCT + FD and DST + FD techniques (i.e. 0.7s and 3.8s respectively), maximum for spline techniques (i.e. app. 32s)).

There are several key areas for future scope. Firstly, our elastographic image generation approach involves manual calculation of certain parameters (such as lateral distances, choosing window sizes and pixel estimates etc.,). We are working to make this automated, so our elastogram technique can work for any data. We are also investigating as to how we can use artificial intelligence (AI) and deep learning techniques to generate more accurate and efficient elastograms.

Our second focus is to integrate compressive sensing [32] into our data acquisition and reconstruction techniques; we are also investigating how we can use AI for efficient data reconstruction and image enhancement, exploring non destructive testing methods [33]. Our techniques were successfully applied on ARFI data, and we obtained better results. So lastly, we will be applying our techniques in other imaging techniques in the field of ultrasound (such as synthetic aperture, focused imaging etc.,)

## REFERENCES

[1] T. Szabo, *Diagnostic Ultrasound Imaging*, 2nd ed., New York, NY, USA: Academic, 2014.

[2] M. Tanter and M. Fink, "Ultrafast imaging in biomedical ultrasound," *IEEE Trans. Ultrason., Ferroelectr., Freq. Control*, vol. 61, no. 1, pp. 102–119, Jan. 2014.

[3] J.-Y. Lu and S. He, "Reducing number of transducer arrays in Fourier image reconstruction method," *IEEE Trans. Ultrason., Ferroelectr., Freq. Control*, vol. 34, no. 6, pp. 1619–1622, 1998.

[4] J.-Y. Lu and S. He, "High frame rate imaging with a small number of array elements," *IEEE Trans. Ultrason., Ferroelectr., Freq. Control*, vol. 46, no. 6, pp. 1416–1421, Nov. 1999.

[5] J. Yu, X. Guo, S. Yan, Q. Le, V. Hingot, D. Ta, O. Couture, and K. Xu, "Randomized channel subsampling method for efficient ultrafast ultrasound imaging," *Meas. Sci. Technol.*, vol. 34, no. 8, Aug. 2023, Art. no. 084005.

[6] A. Delcker, T. Martin, and C. Tegeler, "Magnetic sensor data acquisition for three-dimensional ultrasound of the orbit," *Eye*, vol. 12, no. 4, pp. 725–728, Jul. 1998.

[7] M. U. Din, "Data acquisition system for fingerprint ultrasound imaging device," Electronic thesis, Dept. Elect. Comput. Eng., Univ. Windsor, Windsor, ON, Canada, 2011.

[8] M. N. Ullah, Y. Park, G. B. Kim, C. Kim, C. Park, H. Choi, and J.-Y. Yeom, "Simultaneous acquisition of ultrasound and gamma signals with a single-channel readout," *Sensors*, vol. 21, no. 4, p. 1048, Feb. 2021.

[9] E. Boni, A. Cellai, A. Ramalli, M. Lenge, and S. Ricci, "Multi-channel raw-data acquisition for ultrasound research," in *Proc. 17th Euromicro Conf. Digit. Syst. Design*, Aug. 2014, pp. 647–650.

[10] C. C. P. Cheung, A. C. H. Yu, N. Salimi, B. Y. S. Yiu, I. K. H. Tsang, B. Kerby, R. Z. Azar, and K. Dickie, "Multi-channel pre-beamformed data acquisition system for research on advanced ultrasound imaging methods," *IEEE Trans. Ultrason., Ferroelectr., Freq. Control*, vol. 59, no. 2, pp. 243–253, Feb. 2012.

[11] P.-W. Cheng, C.-C. Shen, and P.-C. Li, "Ultrasound RF channel data compression for implementation of a software-based array imaging system," in *Proc. IEEE Int. Ultrason. Symp.*, Oct. 2011, pp. 1423–1426.

[12] P.-W. Cheng, C.-C. Shen, and P.-C. Li, "MPEG compression of ultrasound RF channel data for a real-time software-based imaging system," *IEEE Trans. Ultrason., Ferroelectr., Freq. Control*, vol. 59, no. 7, pp. 1413–1420, Jul. 2012.
[13] D. Rakhmatov, "Quantization of raw channel data for plane-wave Fourier-domain beamforming," in *Proc. IEEE Int. Ultrason. Symp. (IUS)*, Sep. 2023, pp. 1–5.
[14] K. M. Mohamed and D. M. H. Ali, "Medical B-mode ultrasound imaging reconstruction algorithms: Evaluation and simulation," *Asian J. Converg. Technol.*, vol. 7, no. 3, pp. 51–56, Dec. 2021.
[15] H. Marzougui and D. Rakhmatov, "Data-driven sensor array subsampling for plane-wave ultrasound imaging," in *Proc. IEEE Int. Ultrason. Symp. (IUS)*, Oct. 2019, pp. 2337–2340.
[16] H. A. Akbar and D. Rakhmatov, "Efficient angle selection for coherent plane wave compounding," in *Proc. IEEE Int. Ultrason. Symp. (IUS)*, Oct. 2019, pp. 2355–2357.
[17] D. D'Souza and D. Rakhmatov, "Stratified-medium sound speed profiling for CPWC ultrasound imaging," in *Proc. IEEE Int. Ultrason. Symp. (IUS)*, Sep. 2020, pp. 1–4.
[18] F. Anjidani and D. Rakhmatov, "Efficient ultrasound image enhancement using lightweight CNNs," in *Proc. IEEE Biomed. Circuits Syst. Conf. (BioCAS)*, Oct. 2022, pp. 684–688.
[19] X. Guo, Y. Han, and P. Nie, "Ultrasound imaging algorithm: Half-matrix focusing method based on reciprocity," *Math. Problems Eng.*, vol. 2021, pp. 1–11, Feb. 2021.
[20] S. Dangoury, M. Sadik, A. Alali, and S. Abouzahir, *Ultrasound Imaging: Beamforming Techniques*. Setúbal, Portugal: Scitepress, 2020.
[21] M. Polichetti, F. Varray, J-C. Berra, C. Cachard, and B. Nicholas, "A nonlinear beamformer based on *p*-th root compression—Application to plane-wave ultrasound imaging," *Appl. Sci.*, vol. 8, no. 4, pp. 1–15, Apr. 2018.
[22] M. Albulayli and D. Rakhmatov, "Fourier domain depth migration for plane-wave ultrasound imaging," *IEEE Trans. Ultrason., Ferroelectr., Freq. Control*, vol. 65, no. 8, pp. 1321–1333, Aug. 2018.
[23] D. D. Liu and T.-L. Ji, "Plane wave image formation in spatial–temporal frequency domain," in *Proc. IEEE Int. Ultrason. Symp. (IUS)*, Sep. 2016, pp. 1–5.
[24] A. Rodriguez-Molares, O. M. H. Rindal, O. Bernard, A. Nair, M. A. Lediju Bell, H. Liebgott, A. Austeng, and L. Løvstakken, "The ultrasound toolbox," in *Proc. IEEE Int. Ultrason. Symp. (IUS)*, Sep. 2017, pp. 1–4.
[25] *CIRS QA Spherical Phantom Data Sheet*. [Online]. Available: http://www.cirsinc.com/wp-content/uploads/2019/04/049-049-DS-120418.pdf
[26] G. Montaldo, M. Tanter, J. Bercoff, N. Benech, and M. Fink, "Coherent plane-wave compounding for very high frame rate ultrasonography and transient elastography," *IEEE Trans. Ultrason., Ferroelectr., Freq. Control*, vol. 56, no. 3, pp. 489–506, Mar. 2009.
[27] M. Tanter, J. Bercoff, A. Athanasiou, T. Deffieux, J.-L. Gennisson, G. Montaldo, M. Müller, A. Tardivon, and M. Fink, "Quantitative assessment of breast lesion viscoelasticity: Initial clinical results using supersonic shear imaging," *Ultrasound Med. Biol.*, vol. 34, no. 9, pp. 1373–1386, Sep. 2008.
[28] J. R. Doherty, G. E. Trahey, K. R. Nightingale, and M. L. Palmeri, "Acoustic radiation force elasticity imaging in diagnostic ultrasound," *IEEE Trans. Ultrason., Ferroelectr., Freq. Control*, vol. 60, no. 4, pp. 685–701, Apr. 2013.
[29] S. Konda, "Frequency domain beamforming in acoustical radiation force impulse imaging," Electronic dissertation, Dept. Elect. Comput. Eng., Univ. Victoria, Victoria, BC, Canada, 2021.
[30] W.-S. Lu, "ECE-534 Course: Application of digital signal processing techniques," Dept. Elect. Comput. Eng., Univ. Victoria, Victoria, BC, Canada, Tech. Rep., 2018.
[31] Z. Wang, A. C. Bovik, H. R. Sheikh, and E. P. Simoncelli, "Image quality assessment: From error visibility to structural similarity," *IEEE Trans. Image Process.*, vol. 13, no. 4, pp. 600–612, Apr. 2004.
[32] H. Liebgott, A. Basarab, D. Kouame, O. Bernard, and D. Friboulet, "Compressive sensing in medical ultrasound," in *Proc. IEEE Int. Ultrason. Symp.*, Oct. 2012, pp. 1–6.
[33] J. Camacho, L. Svilainis, and T. G. Álvarez-Arenas, "Ultrasonic imaging and sensors," *Sensors*, vol. 22, no. 20, p. 7911, Oct. 2022.

**SAI KONDA** (Member, IEEE) received the B.Tech. degree from JNTU, Hyderabad, the M.Sc. degree from Wayne State University, Detroit, MI, USA, and the M.Eng. degree from the University of Victoria, Victoria, BC, Canada. He is currently pursuing the Ph.D. degree with the Department of Electronics, Carleton University. His research interests include electronic and medical devices, digital signal processing, and medical image processing.

**HICHAM CHAOUI** (Senior Member, IEEE) received the Ph.D. degree in electrical engineering from the University of Quebec, Trois-Rivières, QC, Canada, in 2011. From 2007 to 2014, he held various engineering and management positions with Canadian Industry. He is currently an Associate Professor with Carleton University, Ottawa, ON, Canada. He is a Registered Professional Engineer in the Province of Ontario. His career has spanned both academia and industry in the field of control and energy systems. His scholarly work has resulted in more than 200 journal and conference publications. He was a recipient of the Best Thesis Award, the Governor General of Canada Gold Medal Award, the Carleton's Research Excellence Award, the Early Researcher Award from the Ministry of Colleges and Universities, and the Top Editor Recognition from the IEEE Vehicular Technology Society. He is an associate editor of several IEEE journals.